Showcasing research from Professor Mingxian Liu's laboratory, School of Chemical Science and Engineering, Tongji University, Shanghai, China.

Unlocking the potential of a multi-electron p-type polyheterocycle cathode: when it meets a small-size and high-charge anion

We design a multi-two-electron p-type polyheterocycle cathode compatible with small-size and high-charge SO_4^{2-} anion. The desirable combination of the two unlocks ultrahigh redox utilization (99.5%) of phenothiazine/piperazine units at ultralow activation energy (0.2 eV), propelling better zinc-organic batteries.

Image reproduced by permission of Mingxian Liu from *Chem. Sci.*, 2025, **16**, 16542.

As featured in:

See Mingxian Liu *et al.*, *Chem. Sci.*, 2025, **16**, 16542.

ROYAL SOCIETY OF CHEMISTRY

15 YEARS ANNIVERSARY

rsc.li/chemical-science

Registered charity number: 207890

Chemical Science

ROYAL SOCIETY OF CHEMISTRY

EDGE ARTICLE

View Article Online
View Journal | View Issue

Check for updates

Cite this: *Chem. Sci.*, 2025, **16**, 16542

All publication charges for this article have been paid for by the Royal Society of Chemistry

Unlocking the potential of a multi-electron p-type polyheterocycle cathode: when it meets a small-size and high-charge anion

Ziyang Song,[ab] Wenbo Liu,[a] Qi Huang,[d] Yaokang Lv,[e] Lihua Gan[ac] and Mingxian Liu *[ac]

Received 7th July 2025
Accepted 12th August 2025

DOI: 10.1039/d5sc05022g

rsc.li/chemical-science

High-voltage p-type organic cathodes are attracting broad attention for boosting zinc batteries, but are hindered by single-electron reactions and low utilization of redox sites due to high reaction energy barriers with incompatible anions. Here we design polyheterocycle organics (PHOs) *via* grafting dual-site-active phenothiazine and piperazine motifs to form donor–acceptor-extended structures which show multi-electron p-type redox reactions for superior anion storage. With the decrease in anionic Stokes radius and the increase in charge density ($TFSI^-$ → OTF^- → SO_4^{2-}), SO_4^{2-} exhibits the strongest bipedal ion-pairing ability with PHOs during oxidation *via* an ultralow activation energy (0.20 *vs.* 0.38 eV of OTF^- and 0.45 eV of $TFSI^-$). This facilitates fast and full utilization of phenothiazine/piperazine active motifs by small-sized and doubly charged SO_4^{2-} anions (99.5% *vs.* 83.2% of OTF^- and 58.1% of $TFSI^-$). Consequently, the PHO cathode delivers superior SO_4^{2-}-storage energy density (317 Wh kg^{-1}) and cycling lifespan (71.4% capacity retention over 100 000 cycles), surpassing OTF^- (273 Wh kg^{-1}/67.1%) and $TFSI^-$ storage (210 Wh kg^{-1}/60.2%), as well as reported p-type organics. This work presents a new paradigm for designing multi-electron organics compatible with optimized anions for better zinc batteries.

Introduction

With the growing demand for sustainable energy storage solutions, aqueous zinc batteries prevail as a leading system, because of resource richness, safe operation, and high capacity of the Zn anode.[1–7] Seeking efficient cathode materials is thus an ongoing task for zinc batteries.[8–12] Benefiting from sustainability, structural flexibility and functional designability, aromatic organic cathode materials are poised for remarkable advancement in Zn-organic batteries (ZOBs).[13–17] The energy storage of organic cathodes is based on n- or p-type redox reactions between electroactive groups and ionic carriers.[18–22] Organic n-type materials (coupling cations, *e.g.*, carbonyl, imine, nitro and azo compounds) often deliver high capacity (>300 mA h g^{-1}) due to their high proportion of redox-active groups.[23–26] However, their low redox voltage (<0.8 V) poses a big challenge for ZOBs.[27,28] In contrast, p-type organics (storing anions) including triphenylamine derivatives and organosulfur compounds exhibit higher redox voltages (>1 V) due to their low electron energy levels, but show low-density active sites and undergo single-electron reactions with limited capacity (generally <200 mA h g^{-1}).[29–33] Although bipolar organics fuse n/p-type characteristics, they face a tricky trade-off between capacity and voltage. Alternatively, in addition to the high voltage merit, p-type organics enable small-sized non-metal anion storage with faster redox kinetics than metallic Zn^{2+} storage in n-type and bipolar organics.[34–38] Consequently, elevating the capacity of high-voltage p-type organics is an efficient approach to significantly boost the energy metrics of ZOBs.

To address the drawback of p-type organics, multi-electron-transfer structure engineering has been demonstrated to provide multiple redox-active sites for boosting the charge storage capacity of ZOBs.[39–41] For example, the Yao group achieved a reversible two-electron-redox process in a phenoxazine cathode, delivering a high capacity of 215 mA h g^{-1} with a redox-site utilization of 73.3% (corresponding to an energy density of ~170 Wh kg^{-1}), which extends the electrochemical horizon of organic cathode materials.[42] Recently, our group proposed a new-type phenoselenazine molecule as the cathode for ZOBs, affording a two-electron-transfer p-type capacity of 227 mA h g^{-1}

[a]*Shanghai Key Lab of Chemical Assessment and Sustainability, School of Chemical Science and Engineering, Tongji University, 1239 Siping Rd., Shanghai, 200092, P. R. China. E-mail: liumx@tongji.edu.cn*

[b]*State Key Laboratory of Pollution Control and Resource Reuse, College of Environmental Science and Engineering, Advanced Research Institute, Tongji University, 1239 Siping Rd., Shanghai, 200092, P. R. China*

[c]*State Key Laboratory of Cardiovascular Diseases and Medical Innovation Center, Shanghai East Hospital, School of Medicine, Tongji University, 150 Jimo Rd., Shanghai 200120, P. R. China*

[d]*Institute for Electric Light Sources, School of Information Science and Technology, Fudan University, 2005 Songhu Rd., Shanghai 200438, P. R. China*

[e]*College of Chemical Engineering, Zhejiang University of Technology, 18 Chaowang Rd., Hangzhou 310014, P. R. China*

Open Access Article. Published on 12 2568. Downloaded on 27/4/2569 23:59:50. This article is licensed under a Creative Commons Attribution-NonCommercial 3.0 Unported Licence.

© 2025 The Author(s). Published by the Royal Society of Chemistry

Open Access Article. Published on 12 2568. Downloaded on 27/4/2569 23:59:50. This article is licensed under a Creative Commons Attribution-NonCommercial 3.0 Unported Licence.

(with an energy density of 273 Wh kg^{-1}), corresponding to 99.2% active-site accessibility.[43] Despite these achievements, the developed p-type organics still suffer from relatively low multi-electron utilization and/or limited anion-accessible capacity due to high spatial reaction barriers.[44,45] Thus, designing p-type organics with both high active site density and high redox utilization for better ZOBs, remains an ongoing yet challenging task.

To this end, almost all reported studies related to ZOBs have focused on the structural design of p-type organic cathodes to elevate multi-electron storage metrics, but have paid less attention to anionic charge carriers in aqueous electrolytes.[46–50] There are three commonly used zinc salts of $ZnSO_4$, $Zn(OTF)_2$ and $Zn(TFSI)_2$ in aqueous ZOBs, based on a trade-off between price, conductivity and interfacial wettability.[51–53] Specifically, p-type organic cathodes are often implemented under one of the above-mentioned electrolyte conditions for ZOBs. Nevertheless, the properties of anions, such as Stokes radius, charge density, ion pair ability and reaction resistance, are also important features for redox kinetics, which may contribute to various electrochemistry processes and energy storage performances.[54] It can thus be rationally anticipated that modulating anionic carriers is highly feasible for altering spatial multi-electron reaction barriers and active-site utilization of p-type organics to boost ZOBs. This raises a key question: what kind of anion carrier is the optimal choice for further unlocking the potential of well-designed p-type organics and leaving room for strategically reforming ZOBs?

In this contribution, multi-two-electron p-type polyheterocycle organics (PHOs) are designed by fusing dual-site-active phenothiazine and piperazine units to form a donor–acceptor-extended polymeric skeleton. PHOs, as the battery cathode, demonstrate an anion-dependent two-electron redox process, delivering a high theoretical capacity of 248 mA h g^{-1}. In different electrolytes, with the decline of anionic Stokes radius and the increase in charge density ($TFSI^- \rightarrow OTF^- \rightarrow SO_4^{2-}$), SO_4^{2-} achieves the strongest bipedal ion-pairing ability during the oxidation reaction, as reflected by its ultralow activation energy (0.20 *vs.* 0.38 eV for OTF^- and 0.45 eV for $TFSI^-$). This enables rapid and full utilization of two-electron phenothiazine/piperazine motifs by small-sized and two-charged SO_4^{2-} anions (99.5% utilization of redox-sites). Therefore, the PHO cathode delivers high SO_4^{2-}-storage energy density and excellent cycling lifespan, surpassing $CF_3SO_3^-$ and $N(CF_3SO_2)_2^-$ storage. This study constitutes a significant advance in the design of multi-electron organics to store compatible anions for advanced ZOBs.

Results and discussion

Benefiting from dual-electron heterocyclic nitrogen/sulfur π-conjugated rings, phenothiazine and phenazine molecules can be considered as desirable multi-electron-transfer cathode materials for high-capacity storage.[55–58] As a consequence, we finely graft two-site-active phenothiazine/phenazine units into stable π-conjugated multi-redox heterocyclic scaffolds, improving their anti-dissolution ability and capacity. Owing to the electron-withdrawing effect of halogen bonds and the electron-donating capability of amine groups, 3,4′,7-tribromo-10-phenylphenothiazinew (TP) and 5,10-dihydrophenothiazine (DP) polymerize in toluene solvent to form PHOs *via* the Buchwald–Hartwig reaction using Ruphos Pd G2, Ruphos and *t*-BuONa catalysts (Fig. 1a). Fourier-transform infrared spectra (FT-IR) exhibit that C–Br groups of TP at 806 cm^{-1} and –NH^- groups of DP at 726 cm^{-1} disappear, accompanied by the formation of C–N species in PHOs at 1234 cm^{-1} (Fig. 1b), confirming the successful fabrication of PHOs.[59] The reduced density gradient diagram (RDG) was simulated,[60] showing obvious green spikes positioned at −0.02–0.01 a.u., indicating strong π–π interactions between adjacent conjugated heterocycles (Fig. 1c). X-ray diffraction (XRD) patterns suggest the amorphous structure of PHOs, where the peak at 27.8° corresponds to the typical π–π stacking interaction between contiguous heterocyclic skeletons (Fig. 1d). Compared with TP and DP molecules (Fig. S1), scanning electron microscopy (SEM) images of PHOs demonstrate particle-clustered morphologies (Fig. 1e), along with porous structures, good thermal stability and uniform atomic distribution (Fig. S2–S4).

Density functional theory (DFT) calculations,[61,62] were applied to reveal the lowest unoccupied molecular orbital (LUMO) and the highest occupied molecular orbital (HOMO) of PHOs. PHOs show a narrow LUMO–HOMO gap (ΔE) of 2.78 eV (Fig. 1f), which facilitates low-energy-barrier electron transfer to start high-kinetics redox reactions. Thanks to the favorable extended π-conjugated structure, PHOs display a low optical bandgap (E_g) of 2.54 eV (Fig. 1g), offering desirable electron delocalization pathways and a high-efficiency charge transfer process.[63] Compared with soluble TP and DP monomers (Fig. 1h), there is no ultraviolet visible (UV-vis) absorption signal for PHOs in $ZnSO_4/H_2O$ solution, confirming their outstanding anti-dissolution capability. Overall, PHOs integrate high-density two-electron redox-active sites, low-energy-bandgap electron delocalization paths, high-voltage p-type heterocycles, and a multi-donor–acceptor-conjugated expanded stable skeleton.

Considering the trade-off between price, conductivity and interfacial wettability, three common zinc salts of $ZnSO_4$, $Zn(OTF)_2$ ($OTF = CF_3SO_3^-$) and $Zn(TFSI)_2$ ($TFSI = N(CF_3SO_2)_2^-$) are often applied in aqueous ZOBs, and their anion properties have an important impact on the electrochemical performance of PHO cathodes in ZOBs. During the oxidation process, the positive charge of the oxidized active group is neutralized by the electrolyte anions through the formation of ion pairs.[64] The ion pairing ability of anions depends on their size and charge distribution around the surface. Molecular dynamics simulations were performed to depict the anionic structures of SO_4^{2-}, OTF^- and $TFSI^-$ in aqueous solvent. Based on their Stokes radii in aqueous solution, the size of the anion increases in the order of SO_4^{2-} (0.296 nm) < OTF^- (0.399 nm) < $TFSI^-$ (0.502 nm) (Fig. 2a). Compared to large anions, small anions often exhibit stronger electrostatic interactions with the oxidized active units of organics. Among these three anions, the dual-charged SO_4^{2-} anion with the smallest Stokes radius also shows a minimized surface molecular electrostatic potential (ESP) value of −11.05 eV (Fig. 2b), which leads to its strongest ion pairing

Open Access Article. Published on 12 2568. Downloaded on 27/4/2569 23:59:50.
This article is licensed under a Creative Commons Attribution-NonCommercial 3.0 Unported Licence.

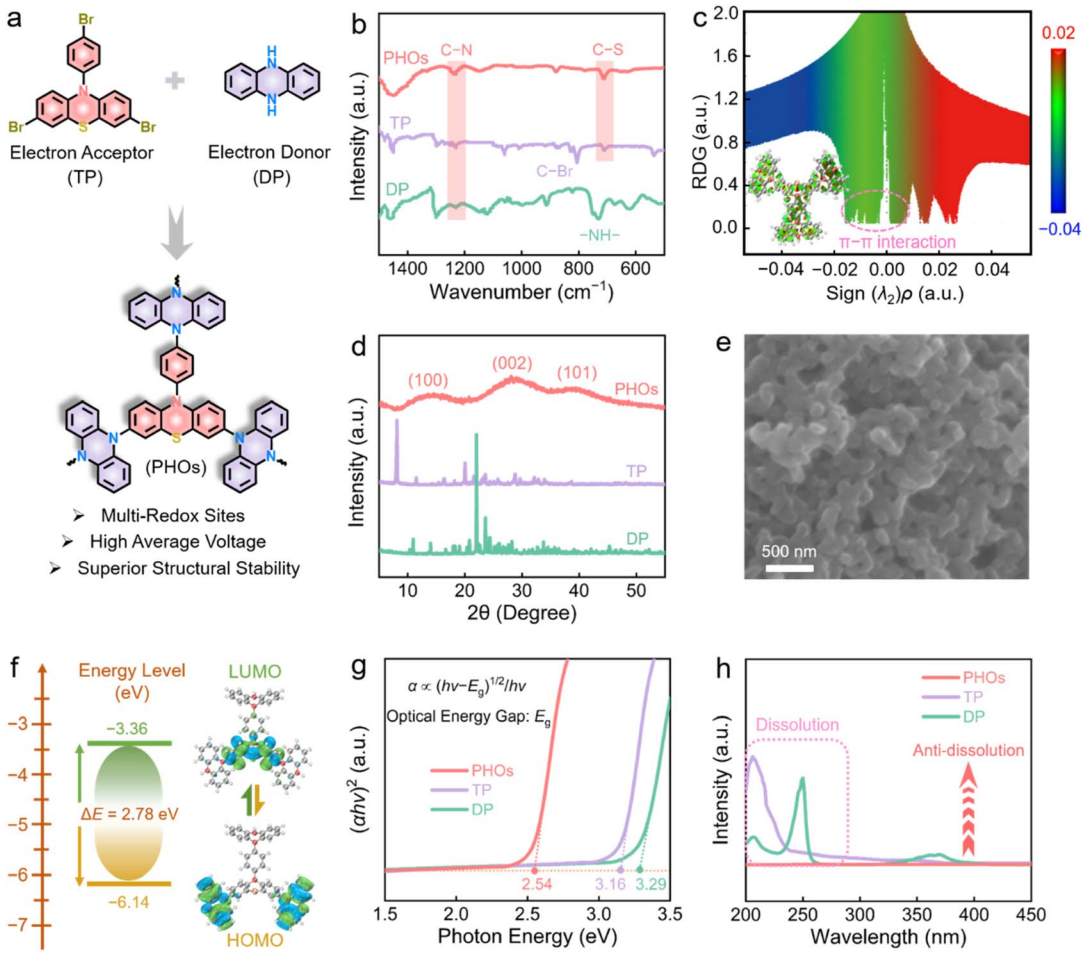

Fig. 1 Structural characterization of PHOs. (a) Synthetic route for PHOs. (b) FT-IR spectra and (c) scatter plots of RDG against sign(λ_2)ρ and the gradient isosurface. (d) XRD pattern. (e) SEM pattern. (f) Energy levels and frontier molecular orbitals. (g) Calculated E_g values. (h) UV/Vis spectra of aqueous $ZnSO_4$ solution soaked with TP, DP and PHOs for three months.

ability with the PHO cathode. When PHOs are oxidized, cationic PHOs can associate with anions to form ion pairs, and the strongest ion pairing ability of dual-charge SO_4^{2-} is conducive to the formation of charge-neutral ion pairs.

In contrast, the formation of ion-pairs between PHOs and $TFSI^-$ is hindered by the steric hindrance of large-sized (0.325 nm) and low-charge (−4.85 eV) $TFSI^-$ anions, which would induce local heterogeneity and then increase redox potential.[65] Thus, small-size and high-charge anions with strong ion-pairing ability can facilitate the oxidation of PHOs, and consequently decrease the redox potential. In contrast, weak ion pairing ability of bulky anions will increase the redox potential of PHOs. Cyclic voltammetry (CV) curves of PHO cathodes in $ZnSO_4$, $Zn(OTF)_2$ and $Zn(TFSI)_2$ electrolytes exhibit two pairs of redox peaks, indicating the existence of a two-step redox charge storage process (Fig. 2c). However, there are some differences in the shapes and redox peaks of CV curves for these electrolytes. Especially, with the decrease in anionic Stokes radius and the increase in charge density ($TFSI^- \rightarrow OTF^- \rightarrow SO_4^{2-}$), two pairs of redox peaks at 1.12/1.42 V and 1.02/1.27 V for SO_4^{2-} are gradually shifted to 1.13/1.46 V and 1.04/1.29 V for OTF^- and 1.16/1.53 V and 1.07/1.39 V for $TFSI^-$ (Fig. 2d).

Besides, electrochemical impedance spectra (EIS) of the PHO cathode at various temperatures (T) exhibit semi-circular patterns with linear tails (Fig. S5). The interface charge transfer resistance (R_{ct}) can be determined by fitting the Nyquist plots based on an equivalent circuit (Fig. S6). A lower R_{ct} value corresponds to rapid interfacial charge conduction, which favors high-kinetics redox reactions of the PHO cathode. The activation energy (E_a) for the interface charge transfer process was determined based on the Arrhenius equation *via* fitting the relationship between R_{ct} and T values.[51] Of note, SO_4^{2-} exhibits the strongest ion-pairing ability during oxidation with an ultralow activation energy of 0.20 eV (Fig. 2e), in comparison to OTF^- (0.38 eV) and $TFSI^-$ (0.45 eV). The lower energy barrier that redox-active groups need to overcome to coordinate with ionic carriers, the more likely the redox reaction is to occur, thereby enhancing the redox kinetics and performances. Overall, these results highlight that the SO_4^{2-} anion, with its small size and high charge density is a desirable charge carrier, is expected to afford superior multi-electron charge storage of the PHO cathode with low energy barriers.

Briefly, as the Stokes radius of the anion decreases and the charge density increases, its ESP value gradually becomes more

© 2025 The Author(s). Published by the Royal Society of Chemistry

Open Access Article. Published on 12 2568. Downloaded on 27/4/2569 23:59:50.
This article is licensed under a Creative Commons Attribution-NonCommercial 3.0 Unported Licence.

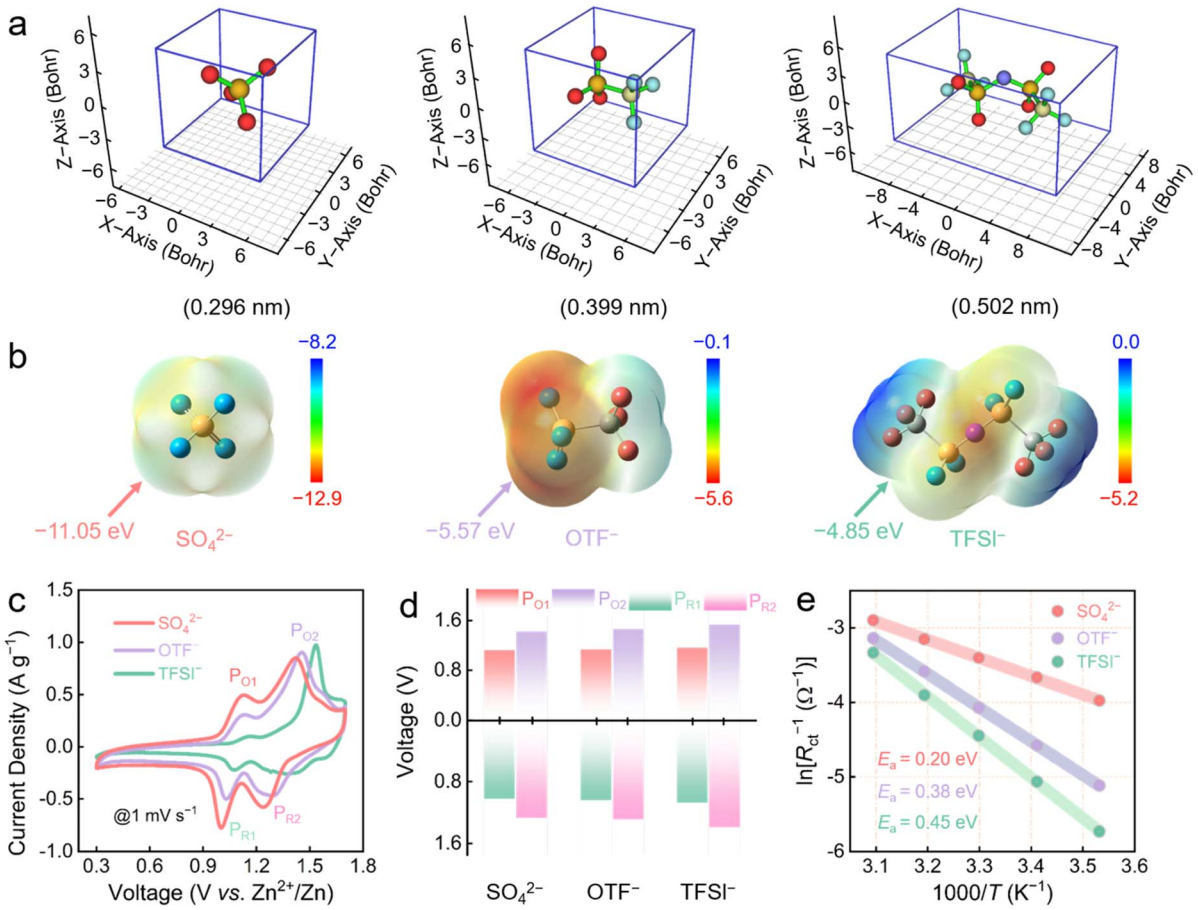

Fig. 2 Electrochemical behavior of PHOs in different electrolytes. (a) Anion size. (b) ESP of the anions. (c) CV curves. (d) Redox peak position. (e) Calculated E_a values of PHOs in SO_4^{2-}, OTF^-, and $TFSI^-$ based electrolytes.

negative (Table S1), indicating stronger ion-pairing ability with organics. This feature contributes to the oxidation of the PHO cathode at reduced redox potentials, which favors achieving superior charge storage in the Zn||PHOs battery with lower energy barriers.

The electrochemical performances of PHO cathodes were investigated in Zn||PHO batteries using zinc foil as the anode and 3 M $ZnSO_4/H_2O$, $Zn(OTF)_2/H_2O$ and $Zn(TFSI)_2/H_2O$ solutions as electrolytes (Fig. S7 and S8). Galvanostatic charge–discharge (GCD) curves of Zn||PHO batteries exhibit two pairs of redox voltage plateaus with a high capacity of 276 mA h g^{-1} at 0.1 A g^{-1} (Fig. 3a), surpassing Zn||TP (73 mA h g^{-1}) and Zn||DP (62 mA h g^{-1}) batteries (Fig. S9). Even at a 500-fold increase in current density to 50 A g^{-1}, the PHO cathode still shows a capacity of 111 mA h g^{-1}, underscoring its strong redox activity and high-rate stability. The differential capacity curve of the Zn||PHO battery displays two pairs of redox signals at 1.11/1.04 and 1.34/1.28 V (Fig. 3b), consistent with CV results obtained during the initial three cycles (Fig. 3c).

In addition, the Zn||PHO battery delivers highly stable and reversible capacities at 0.1–50 A g^{-1} in three electrolytes (Fig. S11). The capacity of the PHO cathode in SO_4^{2-} electrolyte is superior to those in OTF^- and $TFSI^-$ electrolytes (Fig. 3d), highlighting the merits of the size and charge density of SO_4^{2-}. Accordingly, the two-electron-site utilization of PHOs in SO_4^{2-} electrolyte is as high as 99.5% (*vs.* 83.2% in OTF^- and 58.1% in $TFSI^-$). Significantly, the high capacity (276 mA h g^{-1}) and average discharge voltage (1.15 V) endow the Zn||PHO cell with an ultrahigh energy density of 317 Wh kg^{-1}, which is highly competitive with reported organic materials in aqueous batteries (Fig. 3e, S10, and Table S2).[66] Although the capacity of the PHO cathode decreases with increasing current densities due to increased redox resistance (Fig. 3d), it still exhibits highly stable and reversible rate capacities. Benefiting from the donor–acceptor-extended multi-electron polyheterocycle merit, the rate metrics of the PHO cathode are generally superior to those of recently reported organic cathode materials (Table S3), highlighting its high-current redox activity and fast charge transfer kinetics.

More impressively, the Zn||PHO battery in SO_4^{2-} electrolyte shows 100% capacity retention after 5000 cycles at 1 A g^{-1} (Fig. 3f), and achieves an outstanding cycling lifespan of 100 000 cycles with 71.4% capacity remaining at 10 A g^{-1} (Fig. 3g). This excellent cycling life of the Zn||PHO cell exceeds that in OTF^- (67.1%) and $TFSI^-$ (60.2%) electrolytes. Of note, the Zn||PHOs battery achieves 85.5%/81.0% capacity retention at 50 k/60 k cycles, comparable to most recently reported aqueous organic batteries at 50–60 k cycles (Fig. 3h), demonstrating promising

Open Access Article. Published on 12 2568. Downloaded on 27/4/2569 23:59:50.
This article is licensed under a Creative Commons Attribution-NonCommercial 3.0 Unported Licence.

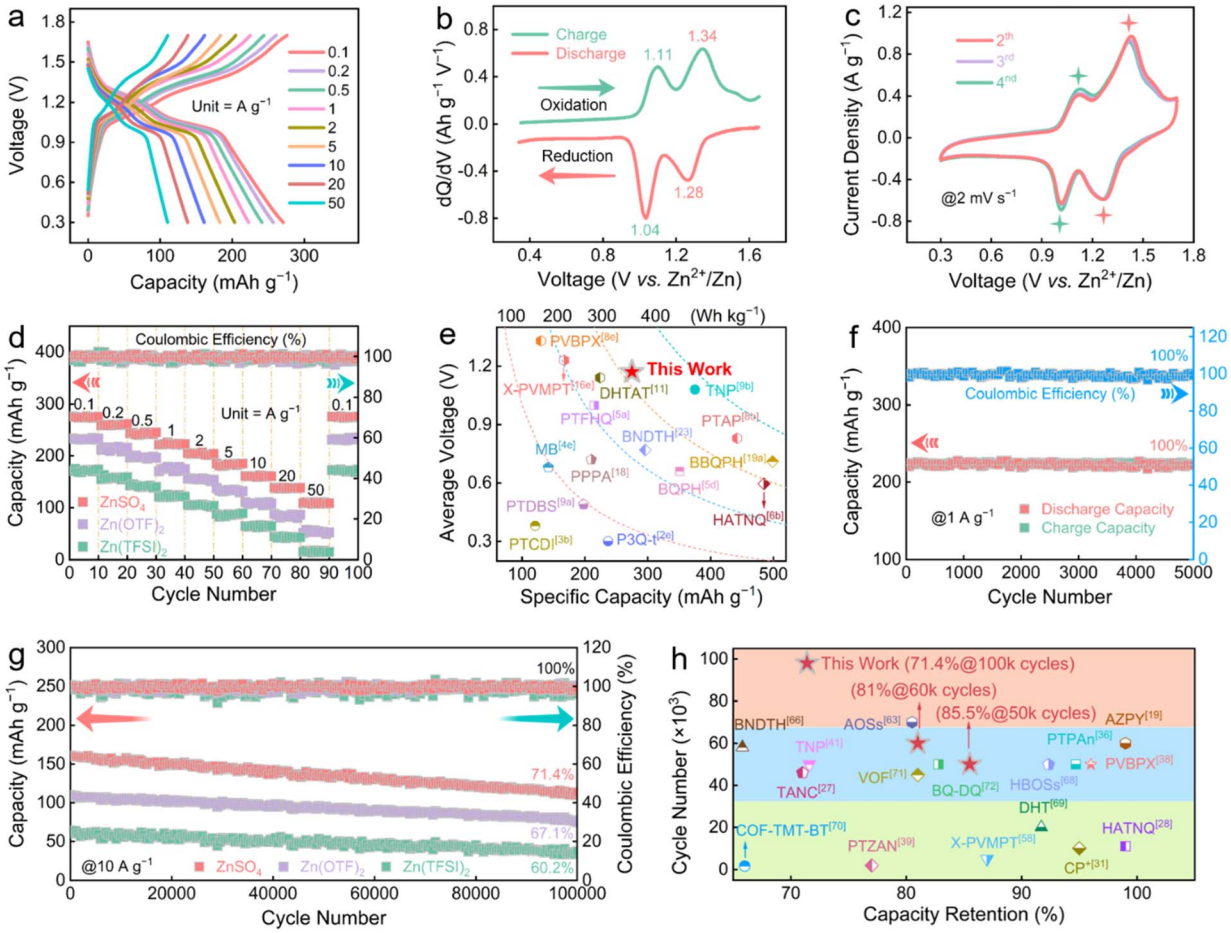

Fig. 3 Electrochemical metrics of the Zn||PHO cell. (a) GCD curves at various current densities. (b) Differential capacity curve. (c) CV profiles. (d) Rate capacities of the PHO cathode in SO_4^{2-}, OTF^-, and $TFSI^-$-based electrolytes. (e) Contour plots of energy density compared with reported organic materials. (f) Cycle stability in SO_4^{2-} electrolyte at 1 A g^{-1}. (g) Long-term cycling performance at 10 A g^{-1}. (h) Life comparison of the PHO cathode with reported organic materials.

practical prospects.[67–72] SEM images, spectral analyses and electrochemical tests of the cycled PHO cathode demonstrate its structural integrity, anti-dissolution property and functional stability with high redox activity (Fig. S12), which can be ascribed to the expanded multi-donor–acceptor polymeric π-conjugated scaffold of PHOs. Inevitably, the repeated plating/stripping reactions of the Zn anode during ultralong-term cycling result in structural degradation and disordered surface geometry to a certain extent (Fig. S13), which poses a limitation to the subsequent operation of the Zn||PHO battery. Given the excellent stability of the PHO cathode, the capacity loss of Zn||PHO cells after cycling can be attributed to the structural degradation of Zn anodes. Overall, the excellent electrochemical metrics of PHOs, including high capacity, average redox voltage, rate performance, superior energy density and ultralong cycle life (Table S3), make it a highly promising cathode material for advanced zinc batteries.

Theoretical calculations were further performed to investigate the oxidation–reduction behaviors of the PHO cathode during the electrochemical process. An optimized heterocyclic plane of PHOs was applied for molecular electrostatic potential (MEP) simulation to visualize electroactive redox sites (Fig. 4a). On the van der Waals surface of PHOs, three piperazine units and one phenothiazine unit (red area) denote p-type electron-donating redox motifs for the bipedal uptake of anionic species. The π-electron localization function map,[73,74] unveils the π-conjugated structure of PHOs, facilitating efficient electron delocalization across the entire framework (Fig. 4b). In the DFT-optimized reaction path, PHOs undergo a two-step 8 e^- bipedal coordination electrochemical process during charging, in which three SO_4^{2-} ions couple with three piperazine units in the first step (step 1), and then a SO_4^{2-} ion reacts with the phenothiazine motif in the second step (step 2). The binding energy (ΔE_b) required for step 1 (−83.22 eV) is lower than that of step 2 (−18.64 eV), confirming that steps 1 and 2 can proceed consecutively (Fig. 4c). During the two-step bipedal coordination process, the formed oxidization products are denoted as PHOs–3SO_4^{2-} (state I) and PHOs–SO_4^{2-} (state II).

Based on the principle of minimum energy, a stable 8 e^- two-step bipedal coordination occurs between the SO_4^{2-} anion and the PHO cathode, corresponding to the two redox voltage platforms of the Zn||PHO cell (Fig. 3a–c). Differential charge

© 2025 The Author(s). Published by the Royal Society of Chemistry

Open Access Article. Published on 12 2568. Downloaded on 27/4/2569 23:59:50.
This article is licensed under a Creative Commons Attribution-NonCommercial 3.0 Unported Licence.

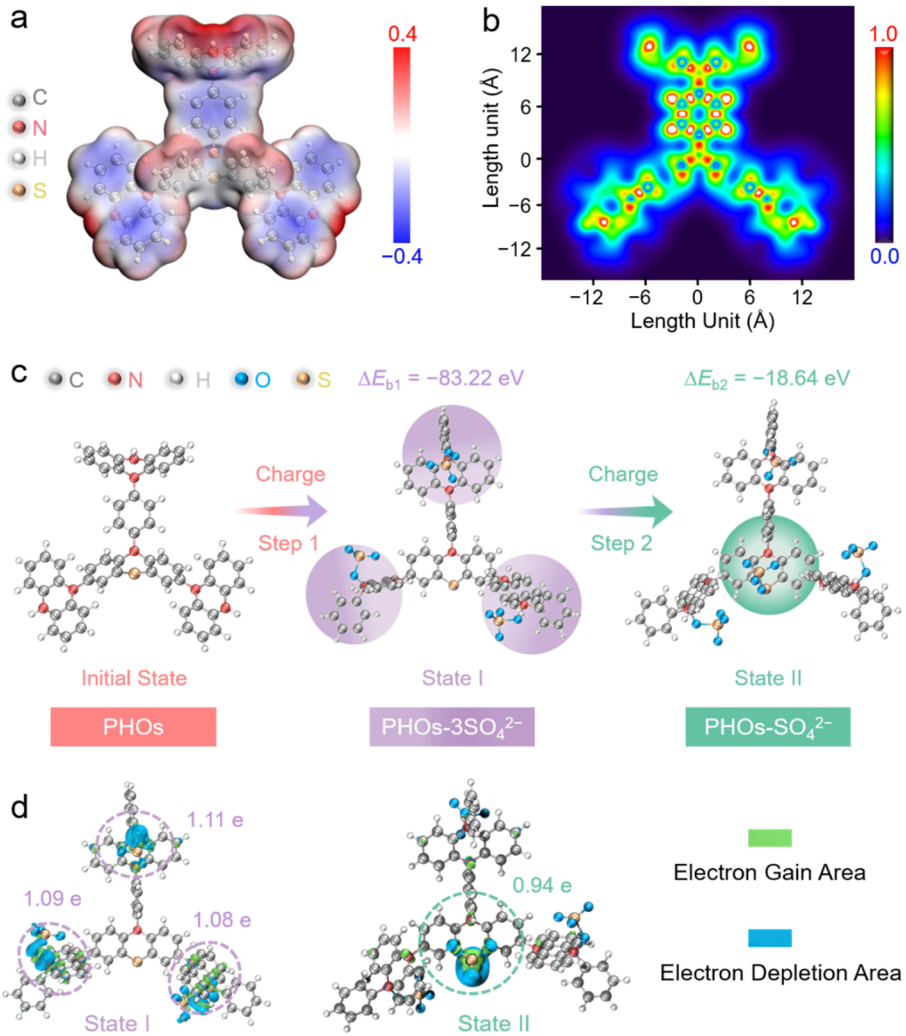

Fig. 4 Theoretical simulations of redox processes of PHOs at various electrochemical states. (a) MEP distribution. (b) ELF-π map. (c) Optimized geometries and corresponding ΔE_b values after ion coordination. (d) Differential charge isosurfaces at state I and II.

isosurfaces,[75,76] were calculated to gain a deeper understanding of the binding properties of SO_4^{2-}-coordinated PHOs (Fig. 4d). According to Bader charge analysis, obvious charge accumulation and depletion areas can be observed between SO_4^{2-} anions and piperazine/phenothiazine units, with significant charge transfers of 1.08–1.11 e at state I and 0.94 e at state II. Such strong redox interactions trigger stable bipedal SO_4^{2-} coordination configurations of PHOs and facilitate full utilization of piperazine/phenothiazine motifs, affording a highly electrochemically active and durable 8 e^- charge storage process of ZOBs.

The structural evolution of the PHO cathode in SO_4^{2-} electrolyte during the charge/discharge process was characterized by FT-IR spectroscopy and X-ray photoelectron spectroscopy (XPS) at five marked potential points of the GCD profile (Fig. 5a). In the FT-IR spectra (Fig. 5b), the C–N moieties of the piperazine units and C–N/C–S of the phenothiazine units easily undergo electrochemical oxidation to loss electrons, transforming into positively charged C=N^+/C=S^+ species for anion uptake. Generally, the peaks of C–N species (1225 cm^{-1}) and C–S bonds (711 cm^{-1}) gradually decrease during charging (state A → C), accompanied by the increase of C=N^+ (1496 cm^{-1}) and C=S^+ (1109 cm^{-1}) species. Such a result indicates the coordination between C–N/C–S bonds and SO_4^{2-} charge carriers. After discharging (state C → E), all the signals come back to their original levels due to the decoordination of SO_4^{2-} anions from redox-active sites. Thus, p-type C–N/C–S motifs of piperazine and phenothiazine modules in PHOs are highly reversible active groups that propel bipedal redox reactions of SO_4^{2-} anions.

XPS spectra of N 1s and S 2p signals were analyzed to delve into the redox behavior of the PHO cathode at various (dis) charged states. For N 1s XPS spectra (Fig. 5c), a distinct peak at 400.1 eV is observed, which corresponds to C–N bonds at state A. During the charging process (state A → C), a new peak emerges at 399.1 eV (representing C=N^+ bond), accompanied by the weakening of the C–N bond at 399.5 eV, indicating the structural evolution from C–N to C=N^+ due to the redox reaction between C–N groups and SO_4^{2-} anions. Conversely, during the discharge process (state C → E), the C–N species reappear due to SO_4^{2-} removal. Regarding the S 2p XPS spectra (Fig. 5d),

Open Access Article. Published on 12 2568. Downloaded on 27/4/2569 23:59:50.
This article is licensed under a Creative Commons Attribution-NonCommercial 3.0 Unported Licence.

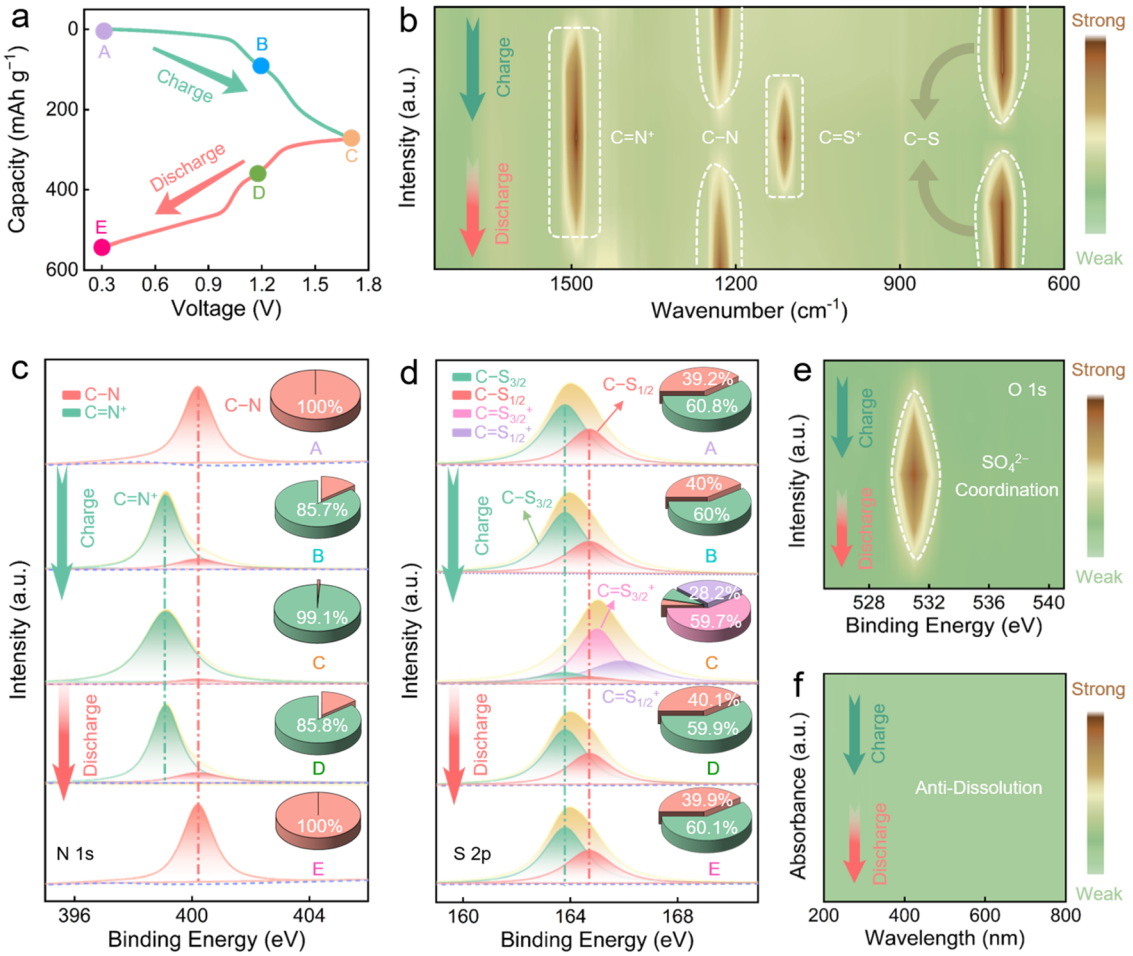

Fig. 5 Structural evolution of the PHO cathode during the operation of the Zn||PHOs cell. (a) A GCD curve. (b) Overview of FT-IR spectra. XPS spectra of (c) N 1s, (d) S 2p, and (e) O 1s at various electrochemical states. (f) UV-vis spectra and photographs of aqueous $ZnSO_4$ electrolyte during (dis)charging.

the C–S species can be fitted into two distinct peaks, C–$S_{3/2}$ (163.8 eV) and C–$S_{1/2}$ (164.7 eV), which remain almost unchanged during charging (state A → B). This indicates that C–S groups are not involved in the redox reaction at this stage. Upon further charging (state B → C), C–S signals shift towards the higher binding energy region and generate new species C=$S_{3/2}$$^+$ at 165.0 eV and C=$S_{1/2}$$^+$ at 165.9 eV, resulting from their coordination with SO_4^{2-} anions. After subsequent discharging (state C → E), all signals return to their original levels because of SO_4^{2-} removal from C–N/C–S sites. These redox behaviors of PHOs are further confirmed by the electrochemical evolution process of SO_4^{2-} anions in O 1s XPS spectra (Fig. 5e).

The dissolution behavior of the PHO cathode in $ZnSO_4/H_2O$ electrolyte at various (dis)charging states was studied *via* UV/Vis spectra. There is no UV/Vis absorption signal (Fig. 5f), which confirms the anti-dissolution ability of PHOs. Of note, colorless $ZnSO_4/H_2O$ solutions soaked with the PHO cathode further prove the structural robustness of PHOs (Fig. S14). Moreover, Zn XPS spectra show no reaction signal of Zn^{2+} cations in the PHO cathode at different electrochemical states (Fig. S15), excluding the participation of Zn^{2+} ions. Besides, the cycled PHO cathode does not show sheet-like zinc hydroxide byproducts, which suggests the insignificant proton contribution in $ZnSO_4/H_2O$ electrolyte (Fig. S16). These findings reveal that SO_4^{2-} anions dominate the two-step 8 e^- charge storage of the PHO cathode, where the C–N groups of three piperazine modules undergo redox reactions first (state A → B and D → E), followed by the C–S motifs of one phenothiazine unit (state B → C and C → D).

Experimental and theoretical studies underline that PHOs initiate a high-kinetics two-step p-type 8 e^- charge storage process during the electrochemical process (Fig. 6a and S17), entailing the stable bipedal coordination of SO_4^{2-} anions with three piperazine motifs (6 e^-) first, followed by one phenothiazine module (2 e^-). Overall, combined with the compatible SO_4^{2-} anions of small size and high-charge density, the PHO cathode with multi-p-type heterocyclic redox-sites, low-activation-energy electron delocalization pathways and extended multi-donor–acceptor-conjugated structures enables state-of-the-art ZOBs with high energy density, superior rate performance, and cycle life.

The redox kinetics of Zn||PHOs cells was investigated based on Dunn's approach.[77] CV profiles at 1–10 mV s^{-1} display two

© 2025 The Author(s). Published by the Royal Society of Chemistry

Open Access Article. Published on 12 2568. Downloaded on 27/4/2569 23:59:50.
This article is licensed under a Creative Commons Attribution-NonCommercial 3.0 Unported Licence.

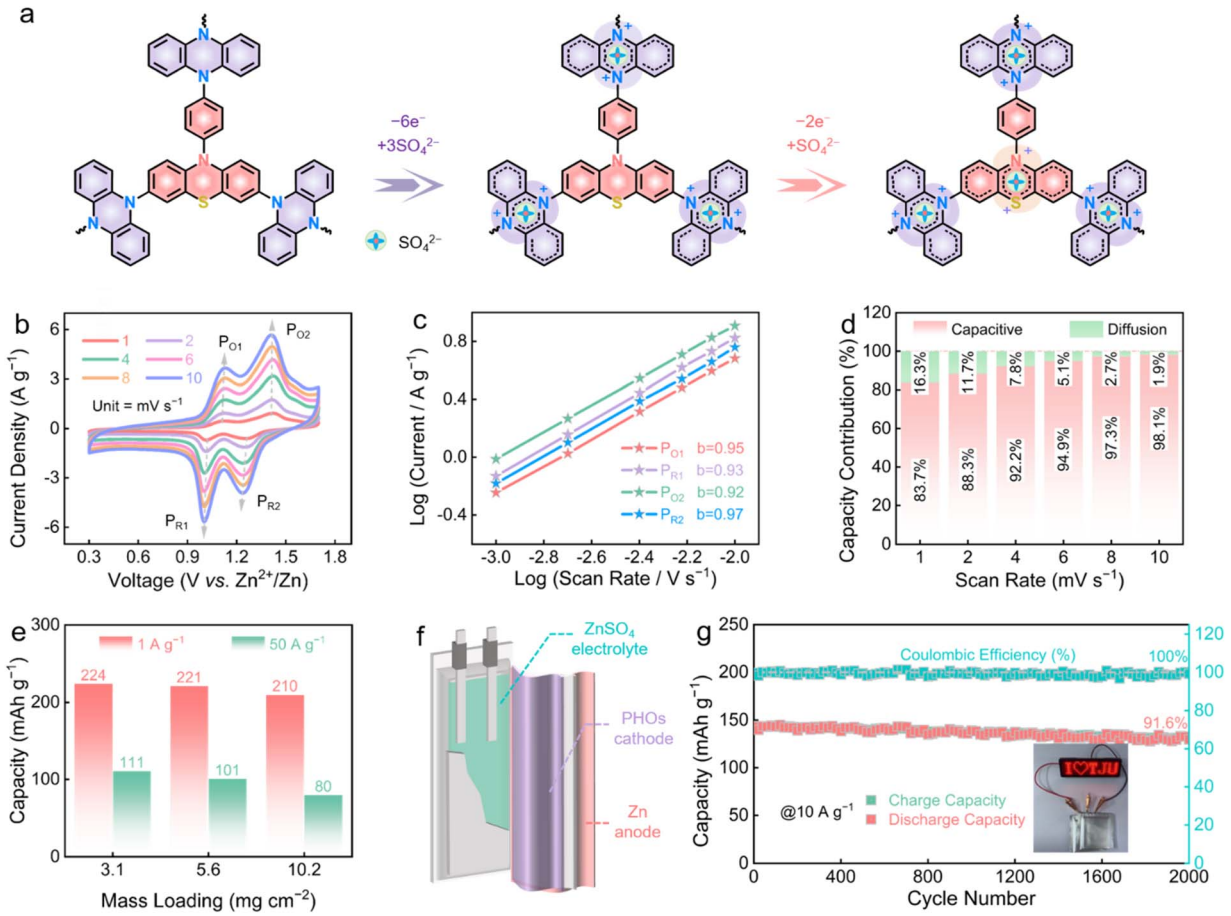

Fig. 6 Charge storage mechanism of the PHO cathode. (a) Two-step bipedal redox behavior of PHOs during the electrochemical charge process. (b) CV curves. (c) Calculated *b* values. (d) Capacitive contribution ratios at different scanning rates. (e) Electrochemical performances of the Zn||PHO battery at the practical-level mass. (f) Schematic diagram of a pouch-type Zn||PHO battery. (g) Cycle stability of the pouch battery at a mass loading of 10.2 mg cm^{-2} for the PHO cathode.

pairs of redox signals with high reversibility, corresponding to two-step piperazine/phenothiazine reactions in the PHO cathode (Fig. 6b). According to the power-law relationship between the peak current (i) and scan speed (v),[78] the power exponent (b) values for four redox peaks are evaluated to be close to 1 (Fig. 6c), indicating a rapid surface pseudocapacitive charge storage process. Compared with the diffusion-controlled process, 92.5% of the total charge storage in PHOs at 4 mV s^{-1} is derived from the surface capacitive contribution (Fig. S18), which further increases to 98.1% at 10 mV s^{-1} (Fig. 6d). Overall, the structural and functional advantages of the PHO cathode are responsible for the fast surface-dominated capacitive charge storage, including multiple dual-active phenothiazine/piperazine motifs, donor–acceptor-extended π-conjugated polyheterocycles, and desirable bipedal ion-pairing ability of small-sized highly charged anions, which enable high SO_4^{2-}-accessibility of redox-active C–N/C–S sites and superior rate capacities.

In view of the excellent performance of the PHO cathode, we investigated its electrochemical potential under high-mass-loading conditions. As the mass loading increases from 3.1 to 10.2 mg cm^{-2}, the capacity gradually decreases, with capacities at 1 A g^{-1} and 50 A g^{-1} retaining 93.8% and 72.1% of their original values (Fig. 6e). We further assembled a Zn||PHO pouch battery (4 × 4 cm^2, Fig. S19) to evaluate its practical application potential. The pouch battery is composed of a PHO cathode, Zn metal anode and 3 M $ZnSO_4/H_2O$ electrolyte (Fig. 6f). The long-term cycling performance of the Zn||PHO pouch battery was tested at 10 A g^{-1}. The battery shows a high capacity of 148 mA h g^{-1} after 2000 cycles, with a capacity retention rate of 91.6% (Fig. 6g). In addition, two series-connected pouch batteries can provide sufficient output voltage to power a lamp plate (inset of Fig. 6g), confirming its good practicality.

Conclusion

In conclusion, multi-electron p-type polyheterocyclic organic materials (PHOs) are rationally designed by fusing dual-site-active phenothiazine and piperazine units, constructing a donor–acceptor-extended polymeric framework. PHOs with a high theorical capacity exhibit an anion-dependent electrochemical behavior and a two-electron redox mechanism. With the decrease in anionic Stokes radius and the increase in charge density ($TFSI^- \rightarrow OTF^- \rightarrow SO_4^{2-}$), SO_4^{2-} achieves the strongest

Open Access Article. Published on 12 2568. Downloaded on 27/4/2569 23:59:50.
This article is licensed under a Creative Commons Attribution-NonCommercial 3.0 Unported Licence.

bipedal ion-pairing ability during the oxidation reaction. This facilitates rapid and stable utilization of multi-electron phenothiazine/piperazine motifs *via* small-sized divalent SO_4^{2-} anions, achieving a redox-site utilization efficiency as high as 99.5%. The assembled Zn||PHO battery delivers state-of-the-art electrochemical performance metrics, including high capacity, desirable average redox voltage, high energy density, and long cycle life. This study will inspire further investigations into highly active organic materials compatible with optimized ions towards advanced energy storage.

Author contributions

M. X. L. conceived the project. L. H. G. and Y. K. L. supervised the research. Z. Y. S. and W. B. L. prepared materials, characterized and analyzed the data. Q. H. performed computational simulations. Z. Y. S., W. B. L., and Q. H. wrote the paper and all authors engaged in discussions related to the manuscript.

Conflicts of interest

The authors declare no conflict of interest.

Data availability

The data that support the findings of this study are available on request from the corresponding author, upon reasonable request.

Supplementary information is available. See DOI: **https://doi.org/10.1039/d5sc05022g**.

Acknowledgements

Z. Y. S., W. B. L., and Q. H. contributed equally to this work. This work was financially supported by the National Natural Science Foundation of China (No. 22272118, 22172111 and 22309134), the Shanghai Rising-Star Program (23YF1449200), the Zhejiang Provincial Science and Technology Project (2022C01182), and the Fundamental Research Funds for the Central Universities.

Notes and references

1 S. W. D. Gourley, R. Brown, B. D. Adams and D. Higgins, *Joule*, 2023, **7**, 1415–1436.
2 C. Han, H. Li, Y. Li, J. Zhu and C. Zhi, *Nat. Commun.*, 2021, **12**, 2400.
3 D. Larcher and J. M. Tarascon, *Nat. Chem.*, 2014, **7**, 19–29.
4 G. Luderer, S. Madeddu, L. Merfort, F. Ueckerdt, M. Pehl, R. Pietzcker, M. Rottoli, F. Schreyer, N. Bauer, L. Baumstark, C. Bertram, A. Dirnaichner, F. Humpenöder, A. Levesque, A. Popp, R. Rodrigues, J. Strefler and E. Kriegler, *Nat. Energy*, 2021, **7**, 32–42.
5 M. Munjal, T. Prein, M. M. Ramadan, H. B. Smith, V. Venugopal, J. L. M. Rupp, I. I. Abate, E. A. Olivetti and K. J. Huang, *Joule*, 2025, **9**, 101871.
6 D. Zhang, Z. Song, L. Miao, Y. Lv, H. Duan, M. Li, L. Gan and M. Liu, *Angew. Chem., Int. Ed.*, 2025, **64**, e202414116.
7 W. Du, Q. Huang, X. Zheng, Y. Lv, L. Miao, Z. Song, L. Gan and M. Liu, *Energy Environ. Sci.*, 2025, **18**, 6540–6547.
8 D. Li, Y. Guo, C. Zhang, X. Chen, W. Zhang, S. Mei and C.-J. Yao, *Nano-Micro Lett.*, 2024, **16**, 1.
9 Z. Ma, X. M. Shi, S. I. Nishimura, S. Ko, M. Okubo and A. Yamada, *Adv. Mater.*, 2022, **34**, 2203335.
10 J. C. Zhu, Z. W. Tie, S. S. Bi and Z. Q. Niu, *Angew. Chem., Int. Ed.*, 2024, **63**, e202403712.
11 A. Innocenti, D. Bresser, J. Garche and S. Passerini, *Nat. Commun.*, 2024, **15**, 4068.
12 X. Wang, J. Tang and W. Tang, *Adv. Funct. Mater.*, 2022, **32**, 2200517.
13 J. Lee, H. Lim, J. Park, M. S. Kim, J. W. Jung, J. Kim and I. D. Kim, *Adv. Energy Mater.*, 2023, **13**, 2300442.
14 N. Liu, X. Wu, Y. Zhang, Y. Yin, C. Sun, Y. Mao, L. Fan and N. Zhang, *Adv. Sci.*, 2020, **7**, 2000146.
15 D. Mecerreyes, N. Casado, I. Villaluenga and M. Forsyth, *Macromolecules*, 2024, **57**, 3013–3025.
16 M. X. Yu, Y. H. Liu, L. Y. Wang, F. C. Cui, B. J. Liu, W. Hu, Y. F. Lu and G. S. Zhu, *Adv. Energy Mater.*, 2024, **14**, 2404008.
17 Q. Zhao, W. Huang, Z. Luo, L. Liu, Y. Lu, Y. Li, L. Li, J. Hu, H. Ma and J. Chen, *Sci. adv.*, 2018, **4**, eaao1761.
18 L. Cheng, X. Yan, J. Yu, X. Zhang, H. G. Wang, F. Cui and Y. Wang, *Adv. Mater.*, 2024, **37**, 2411625.
19 D. Du, Y. Chen, H. Zhang, J. Zhao, L. Jin, W. Ji, H. Huang and S. Pang, *Angew. Chem., Int. Ed.*, 2024, **63**, e202408292.
20 K. W. Nam, H. Kim, Y. Beldjoudi, T.-W. Kwon, D. J. Kim and J. F. Stoddart, *J. Am. Chem. Soc.*, 2020, **142**, 2541–2548.
21 P. Liu, Z. Song, Q. Huang, L. Miao, Y. Lv, L. Gan and M. Liu, *Energy Environ. Sci.*, 2025, **18**, 5397–5406.
22 M. Tang, Q. Zhu, P. Hu, L. Jiang, R. Liu, J. Wang, L. Cheng, X. Zhang, W. Chen and H. Wang, *Adv. Funct. Mater.*, 2021, **31**, 2102011.
23 Q. Q. Sun, T. Sun, J. Y. Du, Z. L. Xie, D. Y. Yang, G. Huang, H. M. Xie and X. B. Zhang, *Angew. Chem., Int. Ed.*, 2023, **62**, e202307365.
24 T. Sun, J. Pan, W. Zhang, X. Jiang, M. Cheng, Z. Zha, H. J. Fan and Z. Tao, *Nano-Micro Lett.*, 2023, **16**, 46.
25 J. Yang, H. Hua, H. Yang, P. Lai, M. Zhang, Z. Lv, Z. Wen, C. C. Li, J. Zhao and Y. Yang, *Adv. Energy Mater.*, 2023, **13**, 2204005.
26 Z. Tie, Y. Zhang, J. Zhu, S. Bi and Z. Niu, *J. Am. Chem. Soc.*, 2022, **144**, 10301–10308.
27 D. Du, J. Zhou, Z. Yin, G. Feng, W. Ji, H. Huang and S. Pang, *Adv. Energy Mater.*, 2024, **14**, 2400580.
28 Y. Chen, J. Li, Q. Zhu, K. Fan, Y. Cao, G. Zhang, C. Zhang, Y. Gao, J. Zou, T. Zhai and C. Wang, *Angew. Chem., Int. Ed.*, 2022, **61**, e202116289.
29 H. Cui, T. Wang, Z. Huang, G. Liang, Z. Chen, A. Chen, D. Wang, Q. Yang, H. Hong, J. Fan and C. Zhi, *Angew. Chem., Int. Ed.*, 2022, **61**, e202203453.
30 D. Kong, T. Cai, H. Fan, H. Hu, X. Wang, Y. Cui, D. Wang, Y. Wang, H. Hu, M. Wu, Q. Xue, Z. Yan, X. Li, L. Zhao and W. Xing, *Angew. Chem., Int. Ed.*, 2021, **61**, e202114681.
31 Y. Yan, P. Li, Y. Wang, L. Bi, T. W. Lau, M. Miao, S. Yang, Q. Xiong, F. R. Lin, H. L. Yip, J. Yin, C. Zhi and A. K. Y. Jen, *Adv. Funct. Mater.*, 2024, **34**, 2312332.

© 2025 The Author(s). Published by the Royal Society of Chemistry

Open Access Article. Published on 12 2568. Downloaded on 27/4/2569 23:59:50. This article is licensed under a Creative Commons Attribution-NonCommercial 3.0 Unported Licence.

32 H. Zhang, L. Zhong, J. Xie, F. Yang, X. Liu and X. Lu, *Adv. Mater.*, 2021, **33**, 2101857.
33 J. Zhang, Y. Wu, M. Liu, L. Huang, Y. Li and Y. Wu, *Angew. Chem., Int. Ed.*, 2023, **62**, e202215408.
34 U. Mittal, F. Colasuonno, A. Rawal, M. Lessio and D. Kundu, *Energy Storage Mater.*, 2022, **46**, 129–137.
35 S. Tang, C. Ye and X. Zhou, *Angew. Chem., Int. Ed.*, 2025, **64**, e202501743.
36 Y. Xiu, A. Mauri, S. Dinda, Y. Pramudya, Z. Ding, T. Diemant, A. Sarkar, L. Wang, Z. Li, W. Wenzel, M. Fichtner and Z. Zhao-Karger, *Angew. Chem., Int. Ed.*, 2022, **62**, e202212339.
37 S. Xu, H. Dai, S. Zhu, Y. Wu, M. Sun, Y. Chen, K. Fan, C. Zhang, C. Wang and W. Hu, *eScience*, 2021, **1**, 60–68.
38 Z. Yang, X. Huang, P. Meng, M. Jiang, Y. Wang, Z. Yao, J. Zhang, B. Sun and C. Fu, *Angew. Chem., Int. Ed.*, 2023, **62**, e202216797.
39 X. Qiu, J. Xu, K. Zhou, X. Huang, M. C. Liao, Y. J. Cao, G. Zhou, P. Wei and Y. G. Wang, *Angew. Chem., Int. Ed.*, 2023, **62**, e202304036.
40 Z. Fu, H. Zhang, D. Geng, Z. Liu, Z. Zhang, X. Li and C. Yan, *Adv. Energy Mater.*, 2024, **14**, 2403934.
41 Y. Fu, Y. Zhang, Q. Huang, P. Liu, Y. Lv, Z. Song, L. Gan and M. Liu, *Mater. Horiz.*, 2025, DOI: **10.1039/D5MH00859J**.
42 J. Ning, X. Zhang, D. Xie, Q. He, J. Hu, J. Tang, R. Li, H. Meng and K. X. Yao, *Angew. Chem., Int. Ed.*, 2024, **63**, e202319796.
43 T. Shi, Z. Song, C. Hu, Q. Huang, Y. Lv, L. Miao, L. Gan, D. Zhu and M. Liu, *Angew. Chem., Int. Ed.*, 2025, **64**, e202501278.
44 A. Duan, Z. Wang, X. Huang and Y. Li, *Angew. Chem., Int. Ed.*, 2023, **62**, e202302754.
45 Y. Zhang, M. Li, Z. Li, Y. Lu, H. Li, J. Liang, X. Hu, L. Zhang, K. Ding, Q. Xu, H. Liu and Y. Wang, *Angew. Chem., Int. Ed.*, 2024, **63**, e202410342.
46 J. Han, A. Mariani, S. Passerini and A. Varzi, *Energy Environ. Sci.*, 2023, **16**, 1480–1501.
47 O. Borodin, J. Self, K. A. Persson, C. Wang and K. Xu, *Joule*, 2020, **4**, 69–100.
48 M. H. Lee, G. Kwon, H. Lim, J. Kim, S. J. Kim, S. Lee, H. Kim, D. Eum, J.-H. Song, H. Park, W. M. Seong, Y. Jung and K. Kang, *ACS Energy Lett.*, 2022, **7**, 3637–3645.
49 Y. Mu, J. Nyakuchena, Y. Wang, J. R. Wilkes, T. Luo, M. Goldstein, B. Elander, U. Mohanty, J. L. Bao, J. Huang and D. Wang, *Angew. Chem., Int. Ed.*, 2024, **63**, e202409286.
50 M. Na, Y. Oh and H. R. Byon, *Chem. Mater.*, 2020, **32**, 6990–6997.
51 Z. Lin, H.-Y. Shi, L. Lin, X. Yang, W. Wu and X. Sun, *Nat. Commun.*, 2021, **12**, 4424.
52 N. Patil, C. de la Cruz, D. Ciurduc, A. Mavrandonakis, J. Palma and R. Marcilla, *Adv. Energy Mater.*, 2021, **11**, 2100939.
53 S. Zheng, D. Shi, D. Yan, Q. Wang, T. Sun, T. Ma, L. Li, D. He, Z. Tao and J. Chen, *Angew. Chem., Int. Ed.*, 2022, **61**, e202117511.
54 Y. Luo, F. Zheng, L. Liu, K. Lei, X. Hou, G. Xu, H. Meng, J. Shi and F. Li, *ChemSusChem*, 2020, **13**, 2239–2244.
55 J. Chen, H. Yin, Q. Xue, J. Zhang, X. Chen, X. Liu, R. He, L. Zhu and F. Wu, *Adv. Funct. Mater.*, 2024, **34**, 2411362.
56 K. Leitonas, A. Tomkeviciene, G. Baratte, A. Dabuliene, S. M. Punniyakoti, D. Volyniuk and J. V. Grazulevicius, *Sens. Actuators, B*, 2021, **345**, 130369.
57 L. W. Luo, C. Zhang, W. Ma, C. Han, X. Ai, Y. Chen, Y. Xu, X. Ji and J. X. Jiang, *Adv. Mater.*, 2024, **36**, 2406106.
58 G. Studer, A. Schmidt, J. Büttner, M. Schmidt, A. Fischer, I. Krossing and B. Esser, *Energy Environ. Sci.*, 2023, **16**, 3760–3769.
59 J. H. Park, M. J. Kwak, C. Hwang, K. N. Kang, N. Liu, J. H. Jang and B. A. Grzybowski, *Adv. Mater.*, 2021, **33**, 2101726.
60 F. Ye, Q. Liu, H. Dong, K. Guan, Z. Chen, N. Ju and L. Hu, *Angew. Chem., Int. Ed.*, 2022, **61**, e202214244.
61 W. Li, H. Xu, H. Zhang, F. Wei, L. Huang, S. Ke, J. Fu, C. Jing, J. Cheng and S. Liu, *Nat. Commun.*, 2023, **14**, 5235.
62 K. Yang, J. Ma, Y. Li, J. Jiao, S. Jiao, X. An, G. Zhong, L. Chen, Y. Jiang, Y. Liu, D. Zhang, J. Mi, J. Biao, B. Li, X. Cheng, S. Guo, Y. Ma, W. Hu, S. Wu, J. Zheng, M. Liu, Y.-B. He and F. Kang, *J. Am. Chem. Soc.*, 2024, **146**, 11371–11381.
63 Z. Song, Q. Huang, Y. Lv, L. Gan and M. Liu, *Angew. Chem., Int. Ed.*, 2025, **64**, e202418237.
64 X. Qu and K. A. Persson, *J. Chem. Theory Comput.*, 2016, **12**, 4501–4508.
65 R. A. Wong, Y. Yokota, M. Wakisaka, J. Inukai and Y. Kim, *Nat. Commun.*, 2020, **11**, 4194.
66 Q. Q. Sun, T. Sun, J. Y. Du, K. Li, H. M. Xie, G. Huang and X. B. Zhang, *Adv. Mater.*, 2023, **35**, 2301088.
67 Y. Zhao, Y. Huang, F. Wu, R. Chen and L. Li, *Adv. Mater.*, 2021, **33**, 2106469.
68 Z. Song, L. Miao, L. Ruhlmann, Y. Lv, L. Li, L. Gan and M. Liu, *Angew. Chem., Int. Ed.*, 2023, **62**, e202219136.
69 C. Ding, Y. Zhao, W. Yin, F. Kang, W. Huang and Q. Zhang, *Angew. Chem., Int. Ed.*, 2024, **63**, e202417988.
70 H. Peng, S. Huang, V. Montes-García, D. Pakulski, H. Guo, F. Richard, X. Zhuang, P. Samorì and A. Ciesielski, *Angew. Chem., Int. Ed.*, 2023, **62**, e202216136.
71 L. Xie, K. Xu, W. Sun, Y. Fan, J. Zhang, Y. Zhang, H. Zhang, J. Chen, Y. Shen, F. Fu, H. Kong, G. Wu, J. Wu, L. Chen and H. Chen, *Angew. Chem., Int. Ed.*, 2023, **62**, e202300372.
72 Y. Zhang, Z. Song, L. Miao, Y. Lv, L. Gan and M. Liu, *Angew. Chem., Int. Ed.*, 2024, **63**, e202316835.
73 L. Lin, Z. Lin, J. Zhu, K. Wang, W. Wu, T. Qiu and X. Sun, *Energy Environ. Sci.*, 2023, **16**, 89–96.
74 T. Sun, W. Zhang, Z. Zha, M. Cheng, D. Li and Z. Tao, *Energy Storage Mater.*, 2023, **59**, 102778.
75 P. Z. Moghadam, Y. G. Chung and R. Q. Snurr, *Nat. Energy*, 2024, **9**, 121–133.
76 W. Humphrey, A. Dalke and a. K. Schulten, *J. Mol. Graphics*, 1996, **14**, 33–38.
77 M. S. Javed, T. Najam, I. Hussain, M. Idrees, A. Ahmad, M. Imran, S. S. A. Shah, R. Luque and W. Han, *Adv. Energy Mater.*, 2022, **13**, 2202303.
78 S. Deng, B. Xu, J. Zhao, C. W. Kan and X. Liu, *Angew. Chem., Int. Ed.*, 2024, **63**, e202401996.

© 2025 The Author(s). Published by the Royal Society of Chemistry